Snow and ice products from Suomi NPP VIIRS

Jeffrey R. Key,[1] Robert Mahoney,[2] Yinghui Liu,[3] Peter Romanov,[4] Mark Tschudi,[5] Igor Appel,[6] James Maslanik,[5] Dan Baldwin,[5] Xuanji Wang,[3] and Paul Meade[7]

Received 28 June 2013; revised 28 October 2013; accepted 3 November 2013.

[1] The Visible Infrared Imager Radiometer Suite (VIIRS) instrument was launched in October 2011 on the satellite now known as the Suomi National Polar-orbiting Partnership. VIIRS was designed to improve upon the capabilities of the operational Advanced Very High Resolution Radiometer and provide observation continuity with NASA's Earth Observing System's Moderate Resolution Imaging Spectroradiometer (MODIS). VIIRS snow and ice products include sea ice surface temperature, sea ice concentration, sea ice characterization, a binary snow map, and fractional snow cover. Validation results with these "provisional" level maturity products show that ice surface temperature has a root-mean-square error of 0.6–1.0 K when compared to aircraft data and a similar MODIS product, the measurement accuracy and precision of ice concentration are approximately 5% and 15% when compared to passive microwave retrievals, and the accuracy of the binary snow cover (snow/no-snow) maps is generally above 90% when compared to station data. The ice surface temperature and snow cover products meet their accuracy requirements with respect to the Joint Polar Satellite System Level 1 Requirements Document. Sea Ice Characterization, which consists of two age categories, has not been observed to meet the 70% accuracy requirements of ice classification. Given their current performance, the ice surface temperature, snow cover, and sea ice concentration products should be useful for both research and operational applications, while improvements to the sea ice characterization product are needed before it can be used for these applications.

Citation: Key, J. R., R. Mahoney, Y. Liu, P. Romanov, M. Tschudi, I. Appel, J. Maslanik, D. Baldwin, X. Wang, and P. Meade (2013), Snow and ice products from Suomi NPP VIIRS, *J. Geophys. Res. Atmos.*, *118*, doi:10.1002/2013JD020459.

1. Introduction

[2] There is now an unprecedented demand for authoritative information on the past, present, and future states of the world's snow and ice resources. The cryosphere, which includes solid precipitation, snow cover, sea ice, lake and river ice, glaciers, ice caps, ice sheets, permafrost, and seasonally frozen ground, exists in various forms at all latitudes and in about 100 countries. It is one of the most useful indicators of climate change yet is one of the most under sampled domains in the climate system.

[1]NOAA/NESDIS, Madison, Wisconsin, USA.
[2]Northrop Grumman Aerospace Systems, Redondo Beach, California, USA.
[3]Cooperative Institute of Meteorological Satellite Studies, University of Wisconsin, Madison, Wisconsin, USA.
[4]Cooperative Remote Sensing Science and Technology Center, City University of New York, New York, New York, USA.
[5]Colorado Center for Astrodynamics Research, University of Colorado, Boulder, Colorado, USA.
[6]IMSG Inc., Rockville, Maryland, USA.
[7]Computational Physics, Inc., Boulder, Colorado, USA.

Corresponding author: J. R. Key, NOAA/NESDIS, 1225 West Dayton Street, Madison, WI 53706, USA. (jkey@ssec.wisc.edu)

2169-897X/13/10.1002/2013JD020459

[3] Changes in the cryosphere have major impacts on health, water supply, agriculture, transportation, freshwater ecosystems, hydropower production, and cryosphere-related hazards such as the floods, droughts, avalanches, and sea level rise. It is therefore not surprising that the cryosphere, its changes, and its impacts have received increased attention in recent years. Today it receives frequent coverage by the media, creating a demand for authoritative information on the state of the world's snow and ice resources from polar ice to tropical glaciers.

[4] Cryospheric observations and information contribute to a variety of societal benefit areas. They help reduce the risk of loss of life and property from natural and human-induced disasters; provide a better understanding of environmental factors affecting human health and well-being; improve the management of energy and water resources including flood forecasting; are required for infrastructure design in cold climates; help us understand, assess, predict, mitigate, and adapt to climate variability and change; improve weather forecasting and hazard warnings; improve the management and protection of terrestrial, coastal, and marine ecosystems; help support sustainable agriculture; and improve our ability to monitor and conserve biodiversity. The performance of numerical weather forecasts strongly depends on the accuracy of initial conditions for predictive models, including snow and ice cover. Ice-mapping services provide forecasts

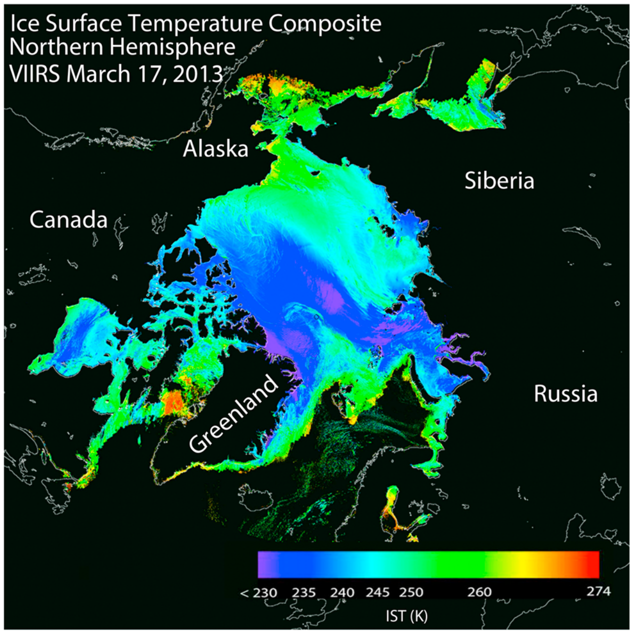

Figure 1. Composite of the VIIRS Ice Surface Temperature EDR over the Arctic on 17 March 2013. VIIRS Land and Cloud Masks are filled as black. Some underestimation of cloud by the VIIRS Cloud Mask occurs in this scene.

for navigation and offshore activities. Cryospheric data play a critical role in climate reanalyses, as input to the assimilation systems and for verification of model fields.

[5] Satellite instruments are essential for delivering sustained, consistent observations of the global cryosphere and are a key to extending local in situ measurements. The Visible Infrared Imager Radiometer Suite (VIIRS) on the Suomi National Polar-orbiting Partnership (S-NPP) satellite provides information that can be used to estimate a number of snow and ice properties. This paper describes the VIIRS snow and ice products. These include the Ice Surface Temperature (IST) Environmental Data Record (EDR), the Sea Ice Characterization EDR, the Sea Ice Concentration intermediate product (IP), and the Snow Cover EDR. The Snow Cover EDR includes two products: a binary snow map and fractional snow cover. The characteristics of these products are described, and preliminary validation studies used to assess the accuracy and utility of the products are presented.

2. S-NPP VIIRS Product Types

[6] The VIIRS instrument was launched on 28 October 2011 as part of the National Polar-orbiting Operational Environmental Satellite System Preparatory Project (NPP). NPP was renamed the Suomi National Polar-orbiting Partnership (S-NPP) soon thereafter. VIIRS was designed to improve upon the capabilities of the operational Advanced Very High Resolution Radiometer (AVHRR) and provide observation continuity with NASA's Earth Observing System's Moderate Resolution Imaging Spectroradiometer (MODIS).

[7] The VIIRS products are processed in the National Oceanic and Atmospheric Administration's (NOAA) near-real time Interface Data Processing Segment (IDPS). The IDPS converts the raw data into calibrated, geolocated Sensor Data Records (SDRs). The SDRs are processed into geophysical parameters called Environmental Data Records (EDRs). In addition to SDRs and EDRs, the IDPS produces Intermediate Products (IPs). While IPs are used in EDR processing, some may be used as stand-alone products. EDRs and IPs are generated in swath-based format. The products are archived and distributed by NOAA's Comprehensive Large Array-data Stewardship System as Hierarchical Data Format 5 format files [http://www.hdfgroup.org/HDF5].

[8] Design features of VIIRS that differ from its heritage instruments include dual gain radiometric bands, the Day-Night Band, and the along-scan aggregation of subpixel detectors to limit pixel growth to an approximate factor of two from nadir to the end of the scan [*Baker*, 2012a]. The pixel sizes at the edge of the scan for VIIRS imagery and moderate resolution bands (0.375 km at nadir; 0.75 km at nadir) are approximately 0.8 km and 1.6 km, respectively, compared to 2.4 km and 4.8 km for MODIS bands (0.5 km at nadir; 1 km at nadir). Furthermore, VIIRS has a wider swath (3000 km) than MODIS (2320 km) [*Hutchison and Cracknell*, 2006].

3. Ice Surface Temperature EDR

[9] Changes in sea ice significantly affect exchanges of momentum, heat, and mass between the sea and the atmosphere. While sea ice extent is an important indicator and effective modulator of regional and global climate change [e.g., *Johannessen et al*., 2004], sea ice temperature and sea ice thickness are the more important parameters from a thermodynamic perspective [*Bitz and Lipscomb*, 1999]. The VIIRS Ice Surface Temperature (IST) EDR provides the radiating, or "skin", temperature at the sea ice surface. It is not strictly an ice temperature; it includes the aggregate temperature of objects comprising the ice surface, including snow and melt water on the ice. Inland water bodies and coastal ice temperatures are available from the land surface temperature EDR. The VIIRS IST EDR (Figure 1) provides surface temperatures retrieved at VIIRS moderate resolution (750 m at nadir), for ice-covered oceans both day and night [*Baker*, 2011a]. The required measurement uncertainty is 1 K over a measurement range of 213–275 K.

3.1. Algorithm Description

[10] The baseline split window algorithm statistical regression method uses two VIIRS infrared (IR) bands, 10.76 μm (M15) and 12.01 μm (M16), for both day and night. It is based on the AVHRR heritage IST algorithm of *Yu et al*. [1995]:

$$\mathrm{IST} = a_o + a_1 T_{\mathrm{M15}} + a_2 (T_{\mathrm{M15}} - T_{\mathrm{M16}}) + a_3(\sec(z) - 1) \quad (1)$$

where T_{M15} and T_{M16} are the VIIRS top-of-atmosphere (TOA) brightness temperatures for the VIIRS M15 and M16 bands, respectively, z is the satellite zenith angle, and a_o, a_1, a_2, and a_3 are regression coefficients. The VIIRS IST algorithm is similar to the IST algorithm first developed by Key and Haefliger [*Key and Haefliger*, 1992; *Key et al*., 1997] for AVHRR. The *Key et al*. [1997] algorithm was later adopted for MODIS [*Hall et al*., 2004].

[11] Pixel level quality flags that provide information such as the cloud confidence, subpixel ice fraction, and other information relevant to retrieval quality are provided with the product and described in detail in the IST Operational Algorithm Description Document [*Baker*, 2013b].

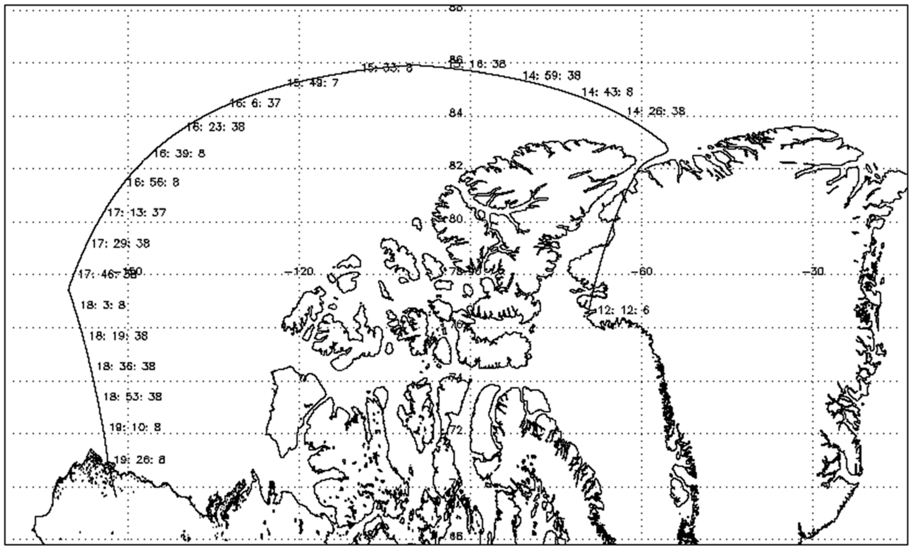

Figure 2. NASA P-3 flight track for 12 March 2012. Times are in UTC.

3.2. Validation

[12] IST EDR performance is dependent upon the quality of the input SDR brightness temperatures, VIIRS Cloud Mask IP cloud confidence, Ice Concentration IP, Aerosol Optical Thickness IP, and regression coefficients derived from matchups between the VIIRS M15 and M16 TOA brightness temperatures and truth surface temperature sources for snow/ice-covered ocean. The IST validation results shown here use prelaunch regression coefficients [*Ip and Hauss*, 2009] derived from global synthetic data [*Baker*, 2012b] that included the effects of VIIRS sensor relative spectral response and sensor noise based on prelaunch test measurement sensor characterization.

[13] Validation of VIIRS IST data is being performed primarily with IST measurements acquired during NASA's Operation IceBridge, which commenced in 2009 and is ongoing, utilizing an aircraft carrying several instruments to measure sea ice and ice sheet characteristics over the Arctic during the spring and the Antarctic in the fall. During March and April 2012, the NASA P-3 aircraft was deployed carrying a Heitronics, Inc. KT-19, which is a downward pointing IR pyrometer that measures the ice surface temperature, though no atmospheric corrections are performed. Figure 2 shows the track of the NASA P-3 aircraft for the 14 March 2012 IceBridge flight. The P-3 flew at an altitude of 300 m over the sea ice during the flight segment analyzed.

[14] Figure 3 shows a comparison between the IST measured by the KT-19, the nearest VIIRS IST measurement, and the MODIS IST product. The MODIS ice surface temperature is retrieved using the algorithm of *Key et al*. [1997]. The comparison is for the flight leg from 16:03:37 to 19:10:08 (west of −120 longitude). The VIIRS overpass occurred from 16:01 to 16:06 UTC and MODIS from 16:35 to 16:40 UTC. IST observations were averaged over 100 points for each VIIRS IST EDR pixel.

[15] Early in 2013, NASA's Land Product Evaluation and Analysis Tool Element reprocessed portions of the VIIRS IST EDR that are coincident with segments of 16 IceBridge flights over sea ice during March and April 2012. The reprocessed VIIRS IST EDR for 14 March 2012 shows very good agreement with the ice surface temperature observed by the KT-19 and with the MODIS IST. Mean ice surface temperature for the 14 March flight track segment, which overlapped 890 VIIRS pixels was −33.24°C for VIIRS, −33.39°C for MODIS, and −33.75°C for the KT-19. An RMS difference of 0.6°C is found between the VIIRS and KT-19 temperatures while MODIS/KT-19 RMS was 1.19°C, and VIIRS/MODIS RMS was 1.12°C.

[16] The Suomi NPP VIIRS ice surface temperature retrievals were also evaluated on a broader scale using collocated ice surface temperature retrievals from MODIS. The MODIS MOD29 product for Terra (MYD29 for Aqua) contains 1 km resolution retrieved ice surface temperature under clear-sky conditions. Suomi NPP and Aqua have similar orbit characteristics, and their ground tracks converge for a few orbits every 2–3 days. For the converged orbits within a time gap of 5 min, ice surface temperature retrievals from MODIS and VIIRS were remapped to a 1 km Polar EASE-Grid using nearest neighbor for the interpolation. An example of the collocated VIIRS IST and MODIS IST on 6 February 2013

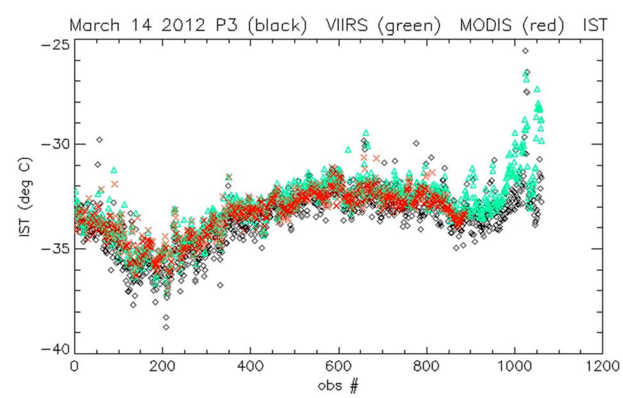

Figure 3. Comparison between the IST (°C) measured by the KT-19 (in black, smoothed over 100 points), the nearest VIIRS IST measurement (in green) and MODIS observation (red). The comparison is for the leg from 16:03:37 to 19:10:08 (west of −120 longitude) on 14 March 2012.

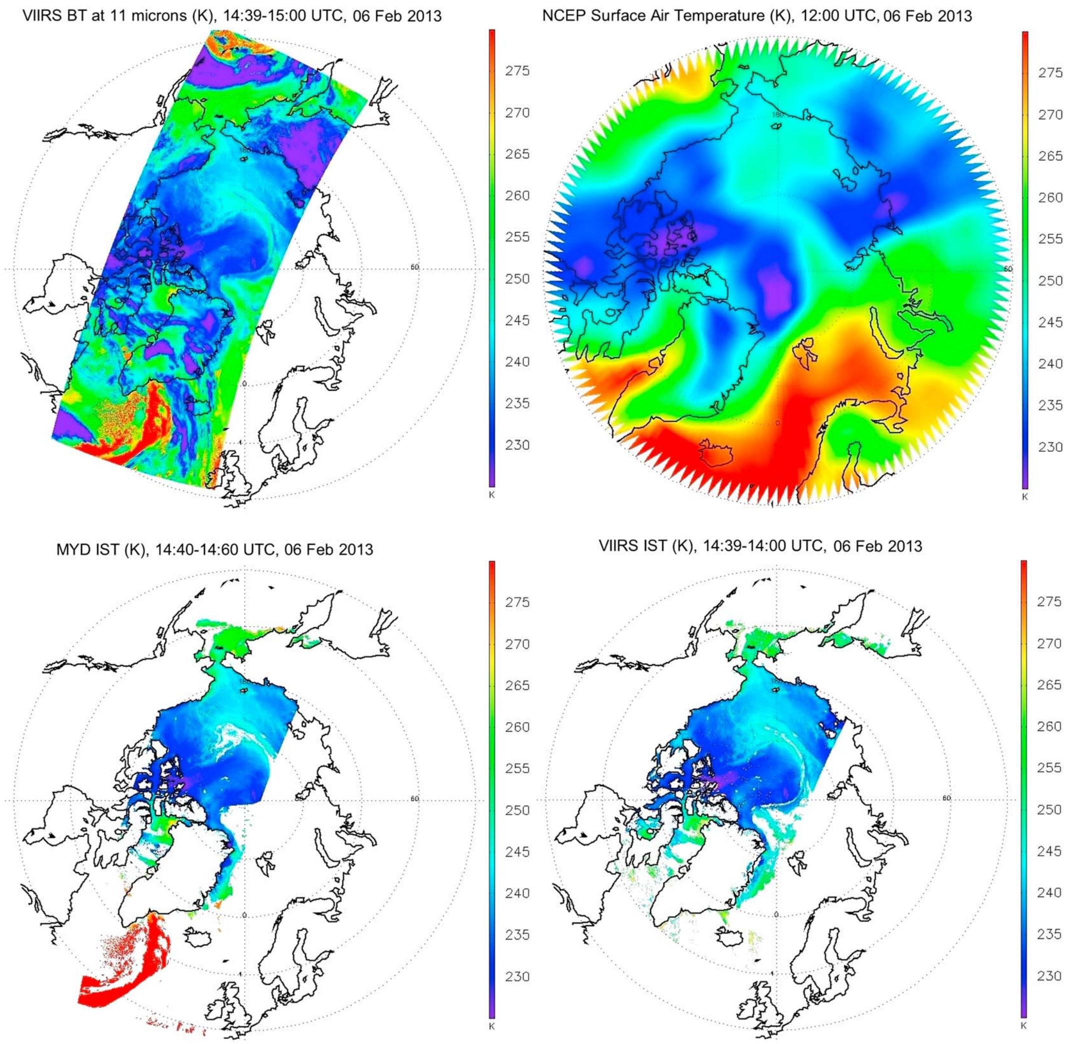

Figure 4. (top left) Suomi NPP VIIRS 11 micron Brightness Temperature, (top right) NCEP surface air temperature, (bottom left) ice surface temperature from Aqua MODIS, and (bottom right) Suomi NPP VIIRS EDR on 6 February 2013.

is shown in Figure 4, with the VIIRS moderate resolution band 15 (M15, 10.76 μm) brightness temperature and 2 m air temperature from the National Centers for Environmental Prediction/National Center for Atmospheric Research (NCEP/NCAR) Reanalysis as reference. The ice surface temperature retrieval over the Arctic Ocean from VIIRS shows similar spatial patterns and values as that from MODIS, and both patterns are similar to that of NCEP/NCAR 2 m air temperature. VIIRS retrievals are available for more pixels due possibly to the cloud leakage (undetected clouds) in VIIRS cloud mask, particularly during nighttime, and MODIS ice surface temperature retrievals include open water at night.

[17] All collocated VIIRS and MODIS Terra and Aqua ice surface temperature retrievals under clear-sky conditions were collected from August 2012 to May 2013 over both the Arctic and Antarctic. In each month, a histogram of ice surface temperature differences of VIIRS and MODIS was plotted for all cases, binned for MODIS ice surface temperature ranges of 213–230 K, 230–240 K, 240–250 K, 250–260 K, and 260–275 K. The bias is defined as the mean of the measurement errors (differences). Measurement uncertainty is defined as the root-mean-square of the measurement errors.

[18] An example of the histogram and statistical analysis in February 2013 is shown in Figure 5. Over 100 million collocated cases were used. The VIIRS ice surface temperature retrievals show the largest negative bias and measurement uncertainty when the surface temperature is close to melting point. With lower surface temperatures, the VIIRS ice surface temperature retrievals show a smaller negative bias and smaller measurement uncertainty. Overall, the measurement uncertainty of VIIRS ice surface temperature retrievals is slightly over 1 K. The performance in other months is similar for both the Arctic and Antarctic.

[19] The IST EDR contains retrievals for false ice. Some of the false ice in the VIIRS Sea Ice Concentration IP has been linked to cloud "leakage" (cloud misidentified as clear) in the VIIRS Cloud Mask (VCM), which is still maturing. IST EDR surface temperature performance bias is relatively small but may improve with updated regression coefficients.

4. Sea Ice Concentration IP

[20] Ice concentration is the fractional area coverage of ice. The VIIRS Sea Ice Concentration IP consists of ice

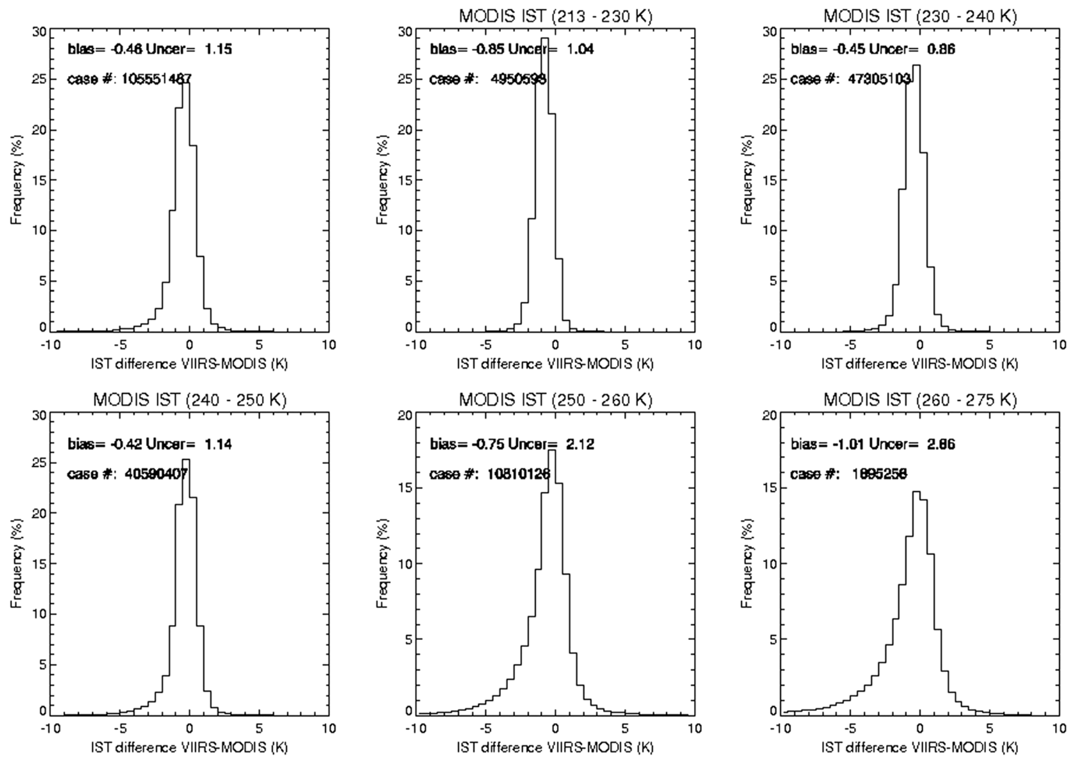

Figure 5. Histogram of ice surface temperature differences of Suomi NPP VIIRS and MODIS (Aqua and Terra) in February 2013 in the Arctic (top left) for all cases and for cases with MODIS ice surface temperature in the ranges 213–230 K, 230–240 K, 240–250 K, 250–260 K, and 260–275 K. Measurement bias (bias) and measurement uncertainty (uncer) are indicated for each bin.

concentration at VIIRS Imagery spatial resolution (375 m at nadir), for both day and night, over oceans poleward of 36°N and 50°S latitude. There are no accuracy requirements for intermediate products.

4.1. Algorithm Description

[21] The Ice Concentration algorithm computes ice fraction based on ice and water tie points determined from VIIRS I1 (0.64 µm) and I2 (0.865 µm) reflectance and surface temperature from the VIIRS Surface Temperature IP which is based on the VIIRS I5 band (11.5 µm):

$$f = \Sigma_j \left[w_j \left(b_j – b_{j,\mathrm{water}} \right) / \left(b_{j,\mathrm{ice}} – b_{j,\mathrm{water}} \right) \right] / \Sigma_j w_j \qquad (2)$$

where f is the calculated ice fraction at pixel, w_j is the relative quality weight in a band, $b_{j,\mathrm{ice}}$ is the ice tie point, $b_{j,\mathrm{water}}$ is the water tie point, and b_j is the pixel reflectance or brightness value for jth source (I1, I2, or Surface Temperature IP).

[22] Ice/water thresholds are determined from the local minimum of the distribution of reflectance and temperature. Ice and water tie points are derived from the local maxima of the reflectance and temperature distribution within a sliding search window centered on each pixel. Ice fraction for each pixel is computed as a quality-weighted average of the fractions independently retrieved for the VIIRS I1 and I2 reflective bands and the Surface Temperature IP. Cloud and quality information are provided by the Ice Quality Flags IP and the Ice Weights IP. Outputs are the Ice Concentration IP and the Reflectance/Temperature IP.

4.2. Validation

[23] The quality of VIIRS sea ice concentration is evaluated using collocated sea ice concentration retrievals from the Special Sensor Microwave Imager/Sounder (SSMIS) onboard the Defense Meteorological Satellite (DMSP) F17 satellite processed with the NASA Team Algorithm [*Comiso et al.*, 1997]. This passive microwave product contains daily sea ice concentrations at a resolution of 25 km for both hemispheres. Collocated sea ice concentration retrievals from VIIRS and the daily passive microwave product are remapped to a 25 km polar EASE-Grid with the nearest neighbor interpolation for the passive microwave data and a weighted average for interpolation for VIIRS.

[24] An example of the collocated VIIRS and passive microwave sea ice concentration on 30 April 2013 is given in Figure 6. The microwave product shows a reduction in the sea ice concentration from the pack ice to the ice edge, while the VIIRS product does not. This difference can be attributed in part to the differences in what the instruments measure (microwave emission versus visible reflectance and thermal emission), instrument field-of-view, and the fundamental differences in the retrieval algorithms. Additionally, sea ice concentration retrievals from passive microwave sensors are less reliable in the presence of melting snow/ice, which is common in the marginal ice zone. The underestimation is shown in Figure 6 when VIIRS and passive microwave sea ice concentration are compared to the sea ice concentration from an operational ice chart. Over Hudson Bay, Hudson Strait, and Davis Strait, both the ice chart and VIIRS show

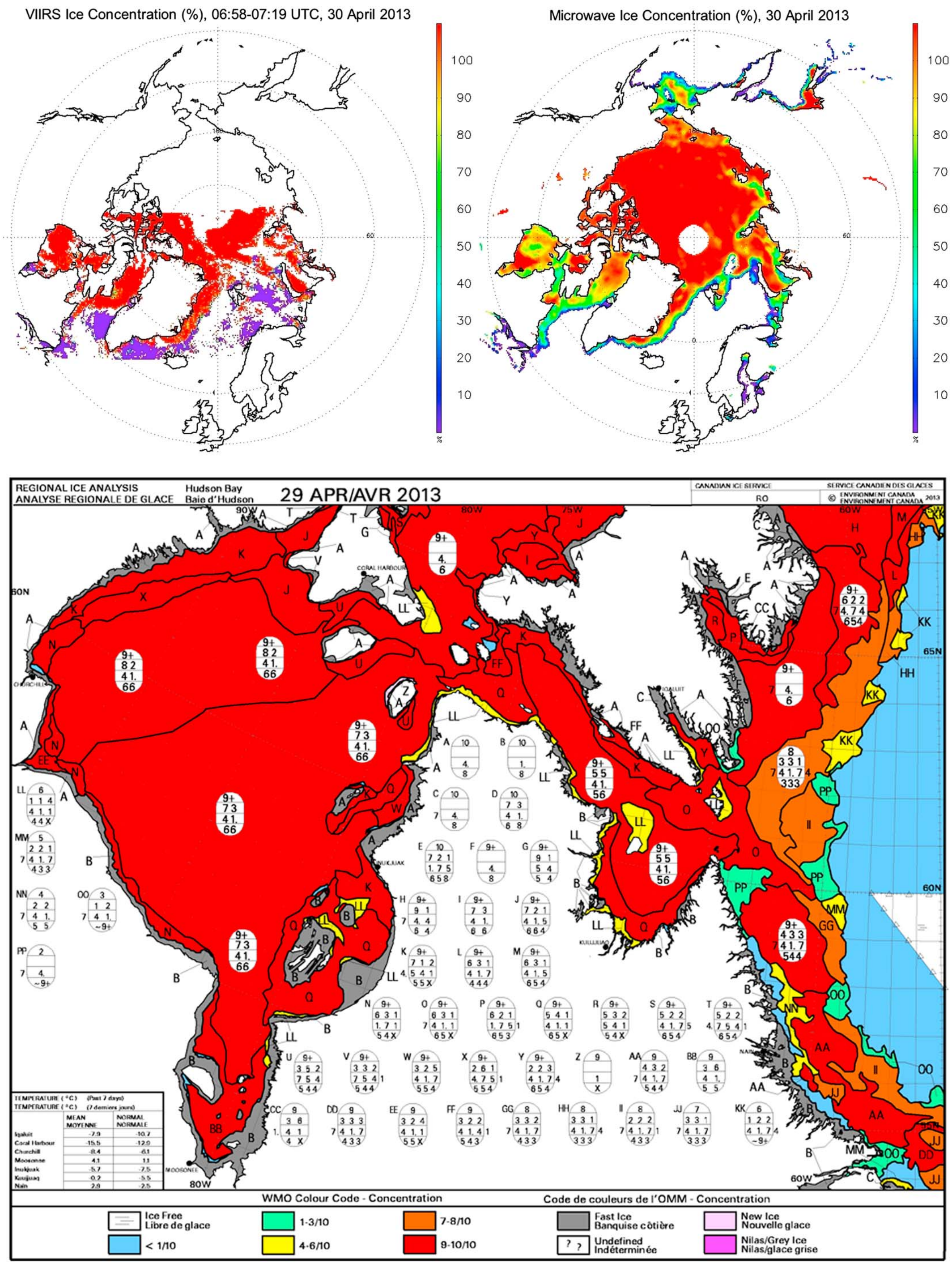

Figure 6. Sea ice concentration (top left) from Suomi NPP VIIRS IP, (top right) from the SSMIS using NASA team algorithm on 30 April 2013, and (bottom) from the Canadian Ice Service weekly ice chart on 29 April 2013.

higher than 90% sea ice concentration, while the microwave product shows sea ice concentrations around 50%. This also explains the large sea ice concentration differences for the intermediate values from microwave product shown in Figure 7.

[25] All collocated VIIRS and passive microwave sea ice concentration retrievals in each month were collected from August 2012 to May 2013 over both the Arctic and Antarctic. In each month, histograms of sea ice concentration differences between the VIIRS and passive microwave products were plotted for all cases and for cases with passive microwave sea ice concentrations in the bins 0–20%, 20–40%, 40–60%, 60–80%, and 80–100%.

[26] An example of the histogram and statistical analysis in February 2013 is shown in Figure 7. Over 200,000 collocated cases were collected in that month. The VIIRS sea ice concentration retrievals show the smallest bias and precision,

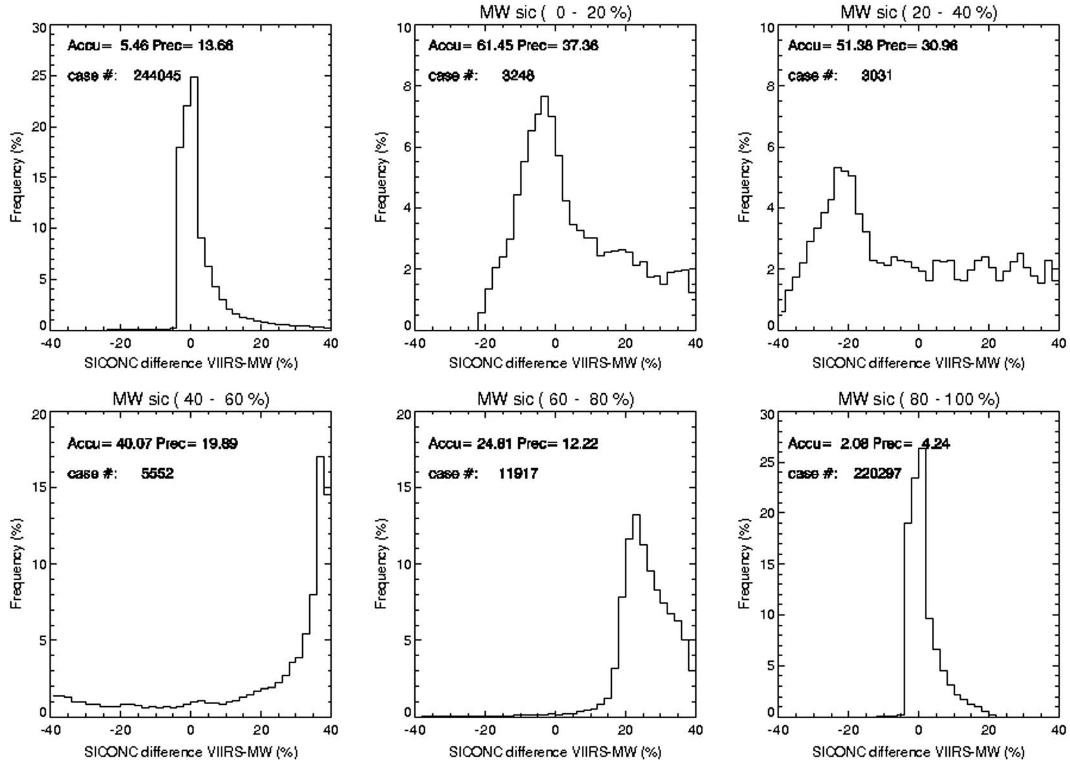

Figure 7. Histogram of sea ice concentration differences of Suomi NPP VIIRS and microwave using NASA team algorithm in February 2013 in the Arctic (top left) for all cases and cases with microwave sea ice concentration in the ranges 0–20%, 20–40%, 40–60%, 60–80%, and 80–100%. Measurement accuracy (bias) and measurement precision (prec) are indicated for each bin.

defined as the standard deviation of the measurement errors, for surface sea ice concentration between 80 and 100%. With lower sea ice concentration, the VIIRS retrievals show larger values of measurement bias and precision. Overall, the measurement accuracy and precision of VIIRS sea ice concentration retrievals are approximately 5% and 15%, respectively. These relatively small values are due to the larger percentage of cases with sea ice concentration between 80 and 100%. In the Arctic, the bias of VIIRS versus passive microwave sea ice concentration are under 10% for most months, while the precision increases from 15% in February to 30% in July. In the Antarctic, the biases increase from 13% in July and August to over 20% in February; and the precision increases from 13% in July to 30% in February. The underestimation of microwave sea ice product for intermediate sea ice concentration may be the main reason for these differences.

[27] Discontinuities with false and missing ice have been observed in transitions from day to night. Nighttime performance is poorer than daytime. The ice concentration performance bias is small but not trivial and may be improved with additional quality checks, algorithm quality checks and maturation of the VCM, and updated Surface Temperature IP regression coefficients.

5. Sea Ice Characterization EDR

[28] Spaceborne sensors, particularly passive microwave radiometers and synthetic aperture radar, have been used primarily to map ice extent and ice concentration and to monitor and study their trends [*Comiso*, 2002; *Maslanik et al*., 2007; *Drobot et al*., 2008; *Comiso et al*., 1997]. Sea ice thickness and volume estimation methods were developed for use with elevation data from the Ice, Cloud and land Elevation Satellite's laser altimeter [*Kwok and Cunningham*, 2008; *Kwok et al*., 2009; *Zwally et al*., 2008], and measurements of sea ice thickness and estimates of sea ice volume have been made using satellite radar altimetry from the recently launched European Space Agency CryoSat-2 mission. Arctic sea ice thickness has also been estimated using airborne radar observations during NASA's IceBridge campaign [*Kurtz et al*., 2013].

[29] The VIIRS Sea Ice Characterization EDR provides an ice age class. VIIRS ice age consists of ice classifications for Ice Free, New/Young, and Other Ice at moderate spatial resolution (750 m at nadir), for both day and night, over oceans poleward of 36°N and 50°S latitude. New/Young ice is discriminated from thicker ice ("Other Ice") by a threshold ice thickness of 30 cm. The accuracy requirement is 70% correct typing of new/young ice, other ice, and ice-free.

5.1. Algorithm Description

[30] There is no operational visible/IR heritage for this product, although there is research heritage using AVHRR [*Massom and Comiso*, 1994; *Yu and Rothrock*, 1996; *Wang et al*., 2010]. Satellite-based passive microwave instruments, such as the DMSP SSM/I, are used to distinguish first year from multiyear ice [e.g., *Comiso et al*., 1997] at much lower spatial resolutions than the VIIRS visible bands provide. Discrimination of new/young ice from thicker ice by the

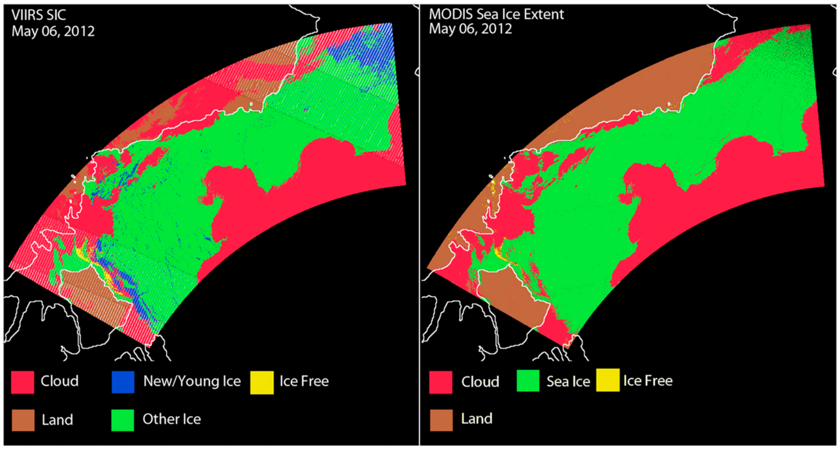

Figure 8. (left) VIIRS Sea Ice Characterization EDR and (right) MODIS Sea Ice Extent over the Beaufort Sea during 6 May 2012.

Sea Ice Characterization EDR is achieved by two algorithms: an energy balance approach [*Yu and Rothrock*, 1996] for nighttime and a reflectance/temperature approach during the day.

[31] The energy (heat) balance method for night and high solar zenith angles is as follows:

$$Q_s = Q_\Sigma(1-\alpha) + E_a – E_s + Q_t + Q_e \quad (3)$$

$$H = \frac{\lambda_i(T-\theta)}{Q_\Sigma(1-\alpha) + E_a - E_s + Q_t + Q_e} - \frac{\lambda_i h}{\lambda_s} \quad (4)$$

where Q_s is the resultant heat flux from the atmosphere to the ice (snow) surface, Q_Σ is total incident short-wave solar radiation, α is the surface albedo, E_a is the long-wave radiation from the atmosphere, E_s is the long-wave radiation from the surface, Q_t is the turbulent heat exchange, Q_e is the heat exchange due to evaporation, H is the ice thickness, h is the snow depth, λ_i is the thermal conductivity of sea ice, λ_s is the thermal conductivity of snow, T_s is the surface temperature, and θ is the freezing temperature of water. In this algorithm, T_s and E_s are computed for each pixel based on an ice "tie point" temperature that is determined from the distribution of VIIRS-retrieved surface temperatures for the local sliding window centered on each pixel. NCEP-gridded surface fields (surface pressure, surface air temperature, specific humidity, and wind speed) are used to determine E_a, Q_t, and Q_e. The incident short-wave solar radiation is determined based on precomputed tables of atmospheric transmittance and solar irradiance using the 6S radiative transfer code [*Vermote et al.*, 1997]. Snow depth for the 30 cm ice thickness threshold is calculated based on the heat/energy balance (equation (4)). The pixel is then classified by comparing the computed snow depth to a climatology look-up table (LUT) snow depth for a 30 cm ice thickness threshold.

[32] The reflectance/ice thickness retrieval method uses a modeled Sea Ice Reflectance LUT for daytime. This daytime (reflectance) algorithm uses ice tie point reflectance from VIIRS I1 and I2 bands, the VIIRS Cloud Mask (VCM) IP, the VIIRS Aerosol Optical Thickness (AOT) IP, and NCEP-gridded precipitable water and total ozone fields. The snow depth for each ice thickness bin is obtained from the modeled snow depth/ice thickness LUT. Ice thickness is estimated from the sea ice reflectance LUT using ice tie point reflectances, modeled snow depth, aerosol optical depth (AOT), precipitable water, and solar and satellite view geometry. A pixel is classified by comparing retrieved ice thickness to 30 cm ice thickness threshold.

[33] Pixel level quality flags that provide information relevant to retrieval quality, such as cloud confidence, are

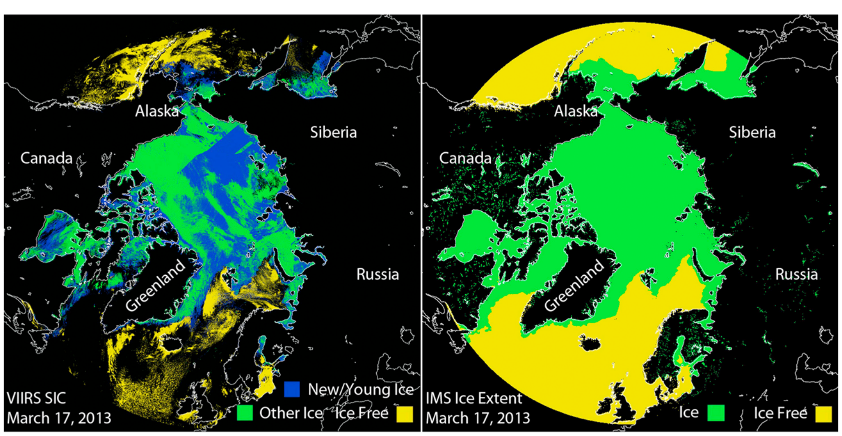

Figure 9. (left) VIIRS Sea Ice Characterization EDR and (right) IMS Sea Ice Extent during 17 March 2013.

Table 1. Comparison Between IMS Sea Ice Extent (ISIE) and VIIRS Sea Ice From Ice Age (VIA) EDR

Comparison Set	Number of Pixels	Percentage
VIA equal to New/Young, Other or Ice Free and ISIE equal to sea ice or Ice Free	1245353	[a]
VIA equal New/Young or other ice	866284	69.6 of valid pixels
ISIE equal to sea ice	805220	64.7 of valid pixels
VIA equal to Ice Free	379069	30.4 of valid pixels
ISIE equal to Ice Free	440133	35.3 of valid pixels
VIA equal to New/Young, or other ice and ISIE equal to sea ice	784581	97.4[b]
VIA equal Ice Free and ISIE equal to Ice Free	358430	81.4[c]

[a]This is the set of valid comparison pixels.
[b]Represents a match between VIA Sea Ice and ISIE Sea Ice, % = (# matching ice pixels/# ISIE ice pixels).
[c]Represents a match between VIA Ice Free and ISIE Ice Free % = (# matching ice-free pixels/ # ISIE ice-free pixels).

provided with the product and described in detail in the VIIRS Sea Ice Age EDR Operational Algorithm Description Document [*Baker*, 2012c].

5.2. Validation

[34] The Sea Ice Characterization (SIC) EDR is being evaluated by examining Northern and Southern Hemisphere large-scale ice classification, as well as more localized regions of interest such as the Beaufort Sea. For example, Figure 8 utilizes the daytime, reflectance threshold branch of the SIC EDR. Ice and ice-free areas agree well, as do the cloud masks from VIIRS and MODIS. The coverage of sea ice appears reasonable, and new/young ice appears in sea ice leads (fractures) and near the coast. However, the appearance of new/young ice in the upper right portion of the image is likely a misclassification, possibly caused my low clouds or fog not identified by the VIIRS Cloud Mask. Note that MODIS does not classify ice type, rather ice and ice-free areas only.

[35] The similarity for ice coverage in the Arctic is evident in Figure 9, which compares the VIIRS SIC sea ice classification using both the daytime and nighttime algorithm branches with ice extent from the Interactive Multisensor Snow and Ice Mapping System (IMS) Daily Northern Hemisphere Snow and Ice Analysis, a 4 km product [*National Ice Center*, 2008]. Table 1 summarizes the agreement for ice and ice-free areas. Although the coverage of ice is in general agreement, inspection of this hemispheric image indicates that new/young ice is considerably overestimated by the VIIRS SIC and with unrealistic spatial patterns. In some cases, the classification is reversed (for example, with thin ice leads classified as other ice, while areas of thicker ice are assigned to the new/young class). Note that the IMS product does not distinguish ice type.

[36] The SIC product was also compared to ice thickness calculated with the One-dimensional Thermodynamic Ice Model (OTIM) of *Wang et al.* [2010]. The OTIM was developed based on the surface energy budget theory. Extensive validation of OTIM has been done with sea ice thickness measurements from submarine cruises, upward looking sonar (ULS) moorings, and in situ measurements in the Arctic Ocean. The overall uncertainty of the OTIM-estimated ice thickness is about 20% for both thin and thick ice [*Wang et al.*, 2010].

[37] The OTIM was applied to VIIRS data to first retrieve sea ice thickness with input clear-sky VIIRS ice surface temperature and ice surface broadband albedo (when available). Sea ice was then classified into ice free, new/young ice, and other ice for comparison to the VIIRS Sea Ice Characterization EDR. Figure 10 shows the Arctic sea ice age from the SIC EDR and from OTIM for 5 May 2013 at 13:50 UTC. Statistical results for this case shown are given in Table 2. Results for other days and for the Antarctic are similar. Overall, the SIC EDR sea ice age classification overestimates

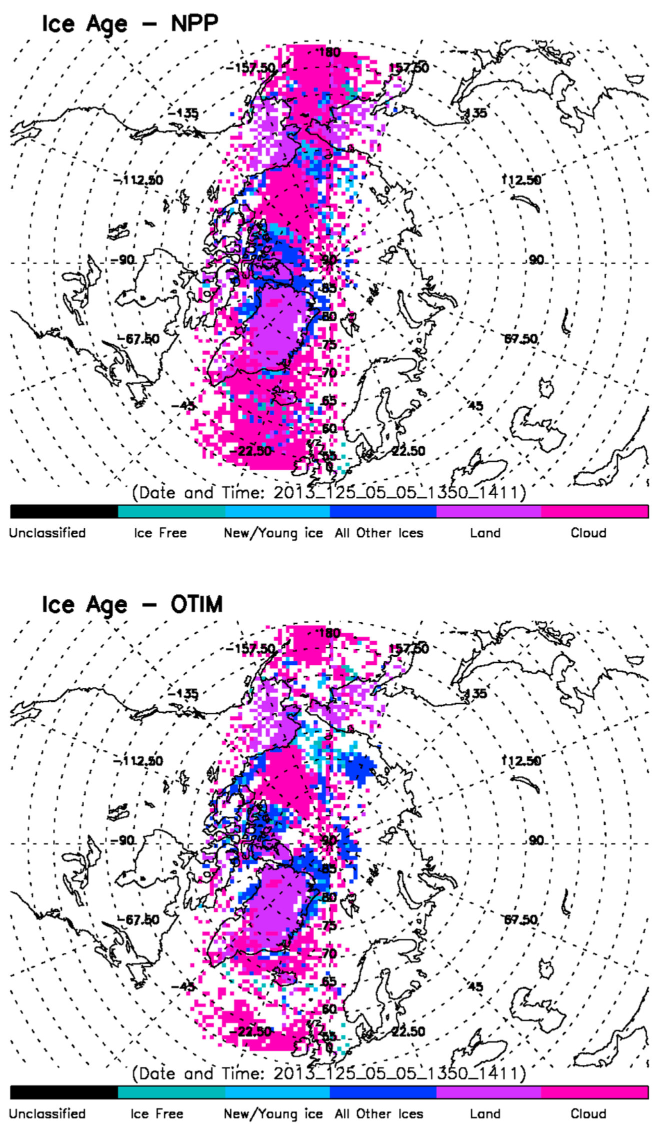

Figure 10. (top) Sea ice age categories from VIIRS sea ice age classification and (bottom) OTIM ice thickness converted to the same categories at 13:50 UTC on 5 May 2013 in the Arctic Ocean. The day/night terminator (90° solar zenith) passes approximately through the center of the image from bottom left to top right.

Table 2. Percentage in Each Ice Age Category From VIIRS and OTIM for Figure 10

Categories	VIIRS Ice Age	OTIM Ice Age	Difference (VIIRS-OTIM)
	Day and night time		
Ice free	17	25	−8
New/Young ice	29	11	18
Other ice	54	64	−10
	Daytime		
Ice free	14	24	−10
New/Young ice	24	5	19
Other ice	62	71	−9
	Nighttime		
Ice free	26	29	−3
New/Young ice	50	25	25
Other ice	24	46	−22

new/young ice percentage and underestimates all other ice percentages, particularly for nighttime conditions, in comparison to OTIM results.

[38] In general, significant discontinuities in ice classification between New/Young and Other Ice have been observed in the granule level mapped composite data. Ice classification discontinuities are most evident near the terminator where the algorithm transitions from the daytime reflectance-based algorithm to the nighttime energy balance algorithm. The snow depth thresholds based on the snow/depth ice thickness climatology LUT are problematic. A possible solution is the use of ancillary precipitation to derive snow depth and compute an ice thickness based on that snow depth. The lower reflectance of melting sea ice appears to cause the SIC EDR to indicate New/Young Ice, although this type of ice cannot be present this time of year.

[39] Future validation of the Sea Ice Characterization EDR will also employ in situ and model data. For example, there are in situ measurements of ice thickness from the New Arctic Program initiated by the Canadian Ice Service in 2002 and sea ice draft measurements from moored ULS instruments in the Beaufort Gyre Observing System. The Pan-Arctic Ice-Ocean Modeling and Assimilation System developed by *Zhang and Rothrock* [2003] simulates the ice thickness distribution, which can also be used for validation.

6. Snow Cover EDR

[40] The VIIRS Snow Cover EDR includes binary (snow/no-snow) and fractional snow cover products. Binary snow cover is derived at 375 m spatial resolution, whereas the spatial resolution of the fractional snow cover product is 750 m. The accuracy requirement for binary snow cover is 90% correct classification. For fractional snow cover the requirement is 10% uncertainty in the fractional snow-covered area over a measurement range of 0–100%. Both products apply to the land surface only under clear-sky conditions.

6.1. Algorithm Description

[41] The VIIRS snow identification algorithm used to generate the binary snow cover product is an adaptation of the heritage MODIS SnowMap algorithm [*Hall et al.*, 2001] that discriminates snow-covered from snow-free pixels. Snow in the VIIRS field of view is identified using a series of threshold tests involving observations in the imagery resolution spectral bands I1 (centered at 0.645 μm), I2 (0.865 μm), I3 (1.61 μm), and I5 (11.45 μm). Besides the observed TOA reflectance and brightness temperatures, the snow identification algorithm uses two spectral indices, the Normalized Difference Snow Index (NDSI) and Normalized Difference Vegetation Index (NDVI), which are calculated from the observed reflectance in the bands I1 (R_{I1}), I2 (R_{I2}), and I3 (R_{I3}):

$$\mathrm{NDSI} = (R_{I1} - R_{I3}) / (R_{I1} + R_{I3}) \tag{5}$$

$$\mathrm{NDVI} = (R_{I2} - R_{I1}) / (R_{I2} + R_{I1}) \tag{6}$$

[42] A pixel in the VIIRS image is considered snow covered if it satisfies the following threshold conditions: NDSI > 0.4, $R_{I2} > 0.11$, and $T_{I5} < 281$ K, where T_{I5} is the brightness temperature observed in the VIIRS band I5. For smaller NDSI values in the range 0.1–0.4, the pixel can still be classified as snow covered if it fits NDVI thresholds determined as a function of NDSI:

$$\mathrm{NDVI\_lower} = a_1 + a_2 * \mathrm{NDSI} \tag{7}$$

$$\mathrm{NDVI\_upper} = b_1 + b_2 * \mathrm{NDSI} + b_3 * (\mathrm{NDVI})^2 + b_4 * (\mathrm{NDVI})^3 \tag{8}$$

where the values of coefficients a_1, a_2, b_1, b_2, b_3, and b_4 are defined following *Klein et al.* [1998].

[43] Adaptations of the heritage MODIS algorithm to VIIRS involved the use of VIIRS TOA brightness temperature (T_{I5}) for thermal false snow screening instead of the estimated land surface temperature in the MODIS algorithm, and the use of VIIRS band 1 reflectance at 0.645μm (R_{I1}) to calculate NDSI instead of the MODIS reflectance at 0.555 μm [*Baker*, 2011b]. To roughly account for the difference between the TOA brightness temperature and the land surface temperature, the brightness temperature threshold in the VIIRS algorithm was lowered slightly as compared to the one used in the MODIS data-processing system (281 K for VIIRS; 285 K for MODIS).

[44] Since most clouds are opaque in the optical and infrared spectral bands, identification of snow in the VIIRS imagery is limited to cloud-clear conditions. Clouds within the VIIRS data-processing system are identified with a separate algorithm [*Baker*, 2013a] prior to the snow mapping. However, rather than a two-category (yes/no) cloud mask, information on the cloud cover is provided with a four-category cloud confidence flag. The four categories of cloud confidence, "confidently cloudy", "probably cloudy", "probably clear", and "confidently clear", allow for generating three different cloud masks and, correspondingly, three different snow cover maps from the same snow cover product. Since the product algorithm theoretical basis document does not explicitly identify what particular cloud mask should be used with the product [*Baker*, 2011b], this may create confusion when evaluating, validating, and comparing the snow-mapping results. In the validation studies described here, VIIRS snow cover maps were generated using the most conservative cloud mask, where all cloud confidence categories except "confidently clear" are considered cloudy, and the snow map is derived only for "confidently clear" areas. A "relaxed" mask incorporating pixels labeled as "confidently cloudy" and "probably cloudy" was also tested but proved to be less accurate than the

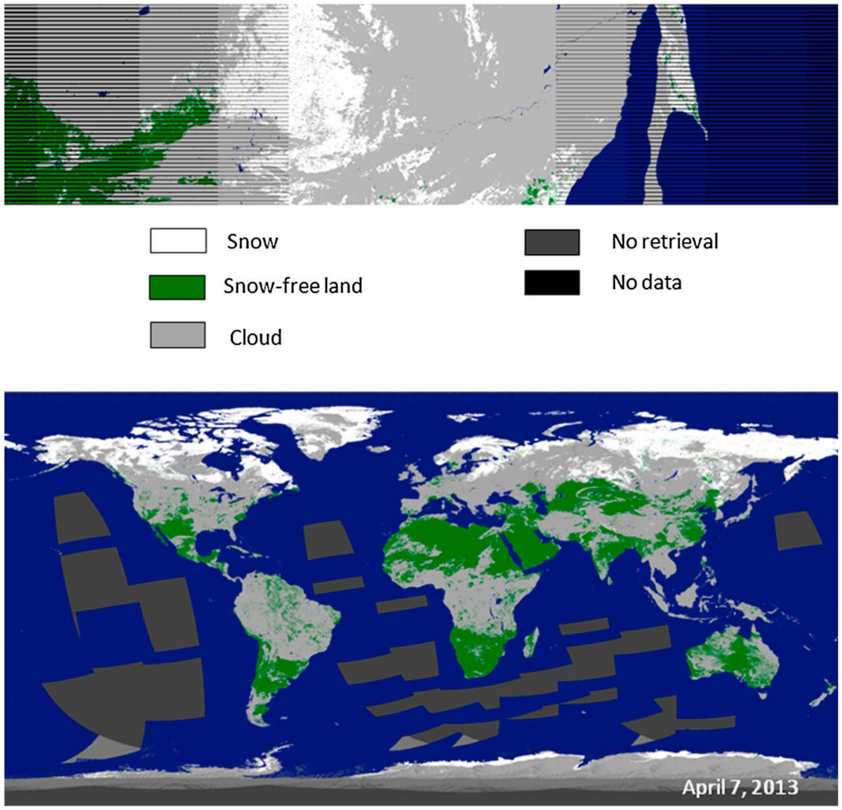

Figure 11. (top) Example of a granule of VIIRS binary snow cover map product with water mask and cloud mask overlaid. Black stripes show dropped portions of scan lines in the granule, the so called "bow tie" effect. (bottom) Daily global snow cover map derived from VIIRS data. Granules containing no "land" pixels are not processed by the VIIRS snow algorithm. This causes gaps in the global snow cover map over ocean areas.

conservative mask. Application of the cloud mask consisting only of "confidently cloudy" pixels resulted in extensive cloud misses and corresponding large snow cover identification errors. Therefore, snow products generated with this latter cloud mask were not considered in this study.

6.2. Validation

[45] Results presented in this section are based on the analysis of VIIRS snow cover binary maps generated during a 6 month period starting in December 2012 and ending in May 2013. Continuous updates and improvements have been made to the VIIRS Cloud Mask algorithm (VCM) since the beginning of VIIRS product generation in early 2012. A VCM algorithm update introduced in November 2012 resulted in significantly improved cloud detection. Data prior to November 2012 were excluded from the analysis due to the substantial variation of performance of the VIIRS Snow Cover EDR associated with evolution of the VCM. In the period from December 2012 to May 2013 both the snow identification and cloud identification algorithms remained essentially unchanged, providing a relatively consistent time series of the snow cover product.

[46] Analysis of the VIIRS snow cover EDR was performed using the VIIRS level 2 (granule-based) snow product. To facilitate the analysis and comparison of VIIRS snow maps with other snow cover products, the original binary snow cover granules were resampled into global latitude-longitude grids with 0.01° (or about 1 km) grid cell size. The nearest neighbor approach was implemented in the resampling process. An example of the snow cover granule and the global daily snow cover map generated with VIIRS data are presented in Figure 11. Gaps in the area coverage of the VIIRS snow map over ocean areas occur because granules with no land pixels are not processed by the system. Due to the large volume of VIIRS data, data processing and analysis was limited to every third day during the time period from December 2012 to May 2013. Overall, the data set included about 60 daily global maps of snow cover derived from VIIRS data.

[47] Different approaches have been used to evaluate the performance of the VIIRS snow-mapping algorithm and to assess the accuracy of the derived binary snow cover maps. For qualitative analysis VIIRS snow cover maps were compared with corresponding false color imagery (Figure 12). For quantitative accuracy assessment the maps were compared with in situ snow observations at ground-based stations. VIIRS maps were also checked for consistency with other satellite-based snow cover products. The latter included snow and ice cover charts generated interactively within NOAA Interactive Multisensor Snow and Ice Mapping System (IMS) [*Helfrich et al.*, 2007] and snow maps derived within an automated approach from MODIS sensor onboard NASA's Terra and Aqua satellites.

[48] Visual examination of the VIIRS snow cover maps in winter and spring of 2012–2013 (Figure 12) has shown that they adequately reproduce major patterns of the global snow

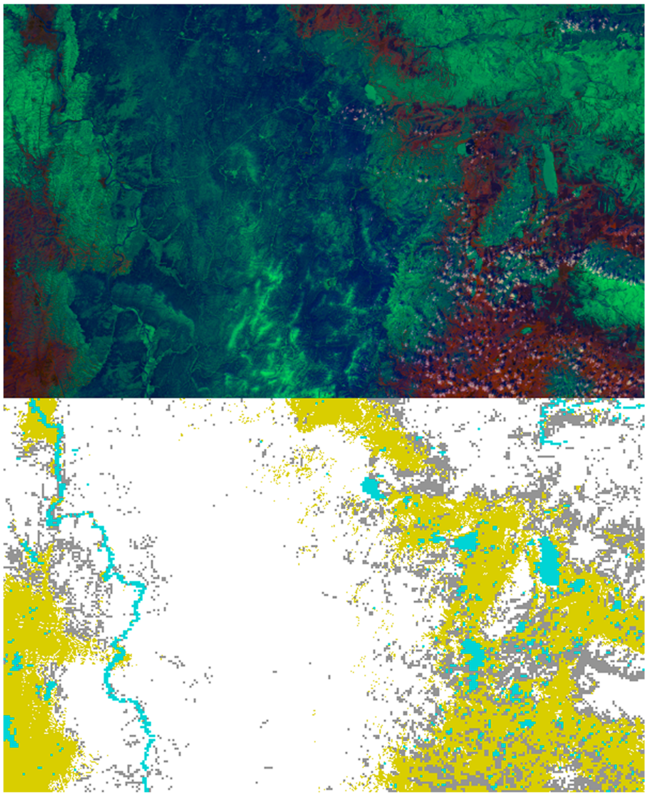

Figure 12. Comparison of (top) false color imagery and (bottom) binary snow retrieval, where white is snow, yellow is non-snow, gray is cloud, and cyan is water, at imagery resolution in swath coordinates for a subset of VIIRS granule observations on 16 April 2013 at 06:20 UTC. The false color image is a combination of VIIRS bands 3 (red), 1 (green), and 5 (blue).

cover distribution and seasonal changes of the snow extent. Most issues found in the VIIRS maps are due to physical limitations of the remote-sensing method involved and are inherent to snow cover maps derived from satellite optical sensor data. Occasional snow misses in the VIIRS snow maps were observed in the boreal forest zones both in Canada and in the Russian Far East due to masking of snow by the forest canopy. The extent of snow misses in the forest had noticeably increased toward late spring. This is explained by an increasing amount of exposed forest litter over the melting snow pack on the forest floor and by reduced reflectance of old melting snow in the visible spectral band. Both factors make the snow cover more difficult to identify.

[49] Snow misses in the VIIRS snow cover map in forested areas are clearly seen in Figure 13, which presents an example of the IMS daily snow cover map over the Northern Hemisphere with the VIIRS snow map overlaid. As compared to VIIRS, IMS analysts tend to identify larger areas as snow covered along the snow cover boundary. Still, the two products demonstrate good agreement on the location of the snow cover boundary in the regions where clouds do not prevent automated snow retrievals.

[50] False snow identifications in the VIIRS snow maps occurred most often in the midst of large cloud masses and were apparently caused by failure of the VIIRS cloud algorithm to properly identify clouds in the instrument field of view. Figure 13 shows patches of snow cover in the midst of clouds identified by VIIRS in the northern part of the Balkan Peninsula in Europe that are quite likely spurious snow. They are located much south of the snow line seen in clear-sky portions of the VIIRS map east and west of this region and contradict with the results of the IMS interactive analysis of the snow cover distribution. Our analysis of VIIRS snow cover maps over low-elevation equatorial regions of South America and Africa that never have a seasonal snow cover has shown that spurious snow cover typically occurs in about 0.08–0.12% of all land pixels. Although the fraction of false snow identification is small, these errors are still noticeable in the global product and thus can lower confidence in the product.

[51] The conterminous United States (CONUS) offers the best opportunity for detailed quantitative validation of VIIRS snow cover maps. Besides several hundred synoptic and airport meteorological stations, reports on the snow depth over CONUS are available from several thousand U.S. Cooperative Network stations (Figure 14). Unlike synoptic stations, U.S. Cooperative stations report zero snow depth when there was no snow on the ground. These reports provide an opportunity to identify both snow omission and commission errors in the satellite product. Synoptic stations in North America and elsewhere in the world issue a missing data report both when the snow depth observation is missing and when there was no snow on the ground. As a result these reports can be used only to identify snow misses in the remote-sensing product. To evaluate the accuracy of blended snow cover maps we directly compared the station data to corresponding grid cells of the snow map. The accuracy was estimated as the fraction of matched satellite-station pairs, where the two products agreed on the state of the snow cover to the total number of matchups.

[52] The comparison of VIIRS-gridded snow cover maps with station data over the CONUS area has demonstrated a close agreement between the two data sets. The time series of the accuracy estimates presented in Figure 14 shows that the rate of agreement between satellite and surface observations of snow cover dropped below 90% for only 1 out of 60 days. For most of the winter season the rate of agreement ranged from 93 to 98%. As seen in Figure 14, in the beginning of the winter season errors were mostly associated with snow misses, whereas in the end of the winter season and in spring most errors were due to false snow identification. The increase in the agreement between the two data sets to almost 100% in late April and in May is not indicative of the true accuracy of VIIRS discrimination of snow-covered and snow-free land surface since at that time the CONUS area was snow free except for a few mountainous locations.

[53] A comparison of VIIRS snow cover maps with NOAA interactive snow charts (IMS) cannot be considered as true validation since the NOAA snow product is based on the analyst's interpretation of the satellite imagery and other ancillary data rather than on direct snow cover measurements. Nevertheless, NOAA charts are generally viewed as the most accurate and reliable source of information on the large-scale snow cover distribution and therefore present a valuable resource for validation of an automated product. Due to coarser, 4 km spatial resolution, IMS maps may not be able to adequately reproduce small-scale peculiarities of the snow cover distribution, particularly in the mountains or in the vicinity of the snow line seen by VIIRS. However,

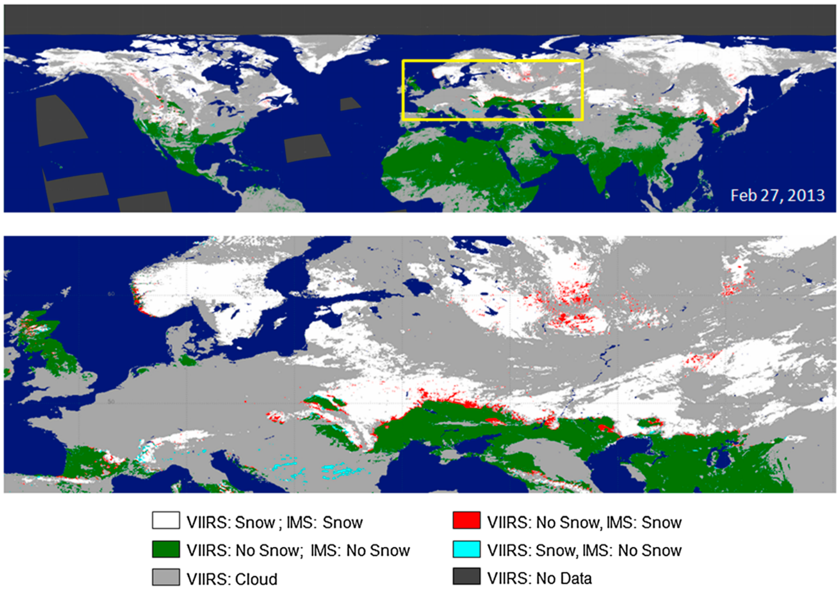

Figure 13. Overlay of the VIIRS daily snow map over the IMS snow product on 27 February 2013. (top) Northern Hemisphere. (bottom) Enlarged portion of the map over Europe.

human involvement in the process of snow map generation practically excludes the occurrence in the IMS of occasional serious snow-mapping errors that are frequently seen in automated products.

[54] To compare IMS charts with VIIRS snow maps, both products were mapped to a latitude-longitude grid with a 0.05° (or about 5 km) grid cell size, also known as the Climate Modeling Grid. IMS charts were resampled to this grid, whereas VIIRS snow map data at 1 km spatial resolution were aggregated within 5 km grid cells. VIIRS grid cells with over 50% of cloudy pixels were assigned a "cloudy" flag, whereas the rest of the land grid cells were labeled as snow covered or snow free according to the dominant category of pixels in the grid cell. "Cloud-clear" 5 km VIIRS snow map grid cells were then compared to corresponding IMS grid cells. Figure 15 gives the results of the quantitative comparison of the VIIRS and IMS daily snow maps over the Northern Hemisphere, demonstrating a close correspondence of the two products.

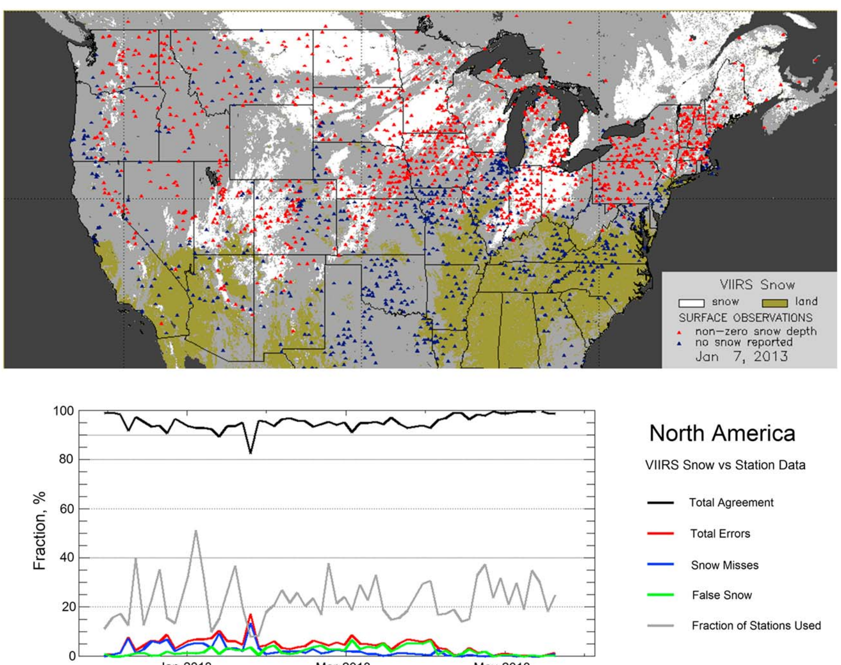

Figure 14. (top) VIIRS binary snow cover map over conterminous U.S. (CONUS) with surface snow cover observation data overlaid. Clouds are shown in gray. (bottom) Statistics of errors and agreement between the VIIRS daily snow cover map and station data during the time period from December 2012 to May 2013. Comparison was performed for every third day during this time period.

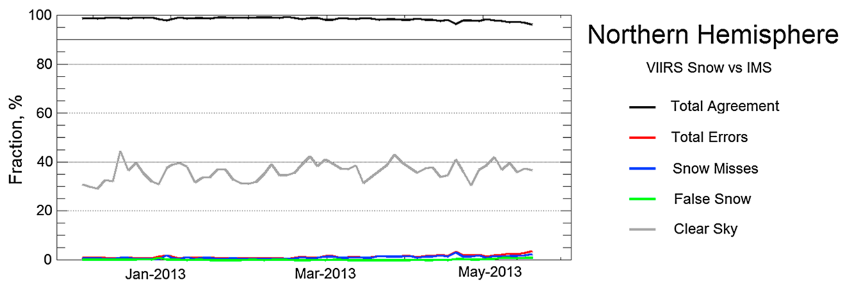

Figure 15. Statistics of errors and agreement between the VIIRS daily snow cover map and IMS snow product for the time period from December 2012 to May 2013. Comparison was performed for every third day during this time period.

The rate of agreement on the snow cover distribution remained above 98% and averaged to about 99% during most of the winter 2012–2013 and in the beginning of spring 2013 but dropped slightly to about 95% in May. A somewhat lower agreement between the two products in late spring may be caused by lower accuracy in the IMS maps. In spring the snow cover melts off earlier than ice on lakes. In the regions having a large number of small water bodies and particularly in the tundra zone IMS analysts frequently interpret this mixture as continuous snow cover and thus overestimate the snow cover extent. It is important to note that comparison between the VIIRS and IMS snow maps was performed only over regions identified in the VIIRS Cloud Mask as "confidently clear".

[55] The accuracy of VIIRS snow cover maps is close to the estimated accuracy of MODIS snow cover maps. Studies comparing MODIS data with in situ observations typically report 93–97% agreement between the two data sets [*Hall and Riggs*, 2007]. Our analysis of the snow map products based on MODIS and VIIRS data, however, has shown that substantially more clouds are mapped in the VIIRS snow map than in the MODIS product. The fraction of pixels identified as cloudy in the MODIS snow map is typically 55–60% [e.g., *Wang et al*., 2008], whereas in the VIIRS snow product the fraction of cloudy pixels identified with the conservative cloud mask is 65–70%. As a result, the effective daily area coverage of current VIIRS snow maps was substantially smaller than that of MODIS.

[56] A comprehensive analysis of the reasons for overestimation of the cloud amount by the VIIRS cloud identification algorithm falls beyond the scope of this study. Still, one of these reasons is clearly the tendency of the VIIRS cloud algorithm to interpret shallow and patchy snow cover under clear-sky conditions as a cloudy scene. As a result, areas in the vicinity of the snow line corresponding to the transition from completely snow-covered land surface to completely snow free are frequently mapped in the VIIRS snow cover map as cloudy. Since most disagreement between the satellite and in situ snow observations occurs in the transition zone, mapping it as cloudy and therefore eliminating it from the comparison increases the estimated accuracy of the satellite snow cover product. The conservative nature of the cloud mask should therefore be accounted for in the overall evaluation of the quality of the satellite-based snow cover map along with its accuracy. However, quantitative criteria that would incorporate both parameters have yet to be developed.

[57] Validation of VIIRS snow cover maps was limited to the Northern Hemisphere. Comprehensive evaluation of snow cover product over the Southern Hemisphere is not currently possible, as snow cover over Southern Hemisphere is not mapped interactively within IMS and there are only a few ground stations in South America routinely delivering reports on snow cover. Given that the same algorithm is applied globally, it is reasonable to assume that the accuracy of snow maps over the Southern Hemisphere will be similar to that for the Northern Hemisphere.

[58] In the current version of the VIIRS product generation system, the snow fraction product is calculated by aggregating the binary snow cover data within 2×2 pixel cells. Hence, the fractional snow cover product is a direct derivative of the binary snow cover product with little added value. While case studies have shown that the fractional snow cover product may meet the accuracy requirement overall, it does not meet the requirement throughout the measurement range because only five snow fraction values are possible (0, 25, 50, 75, and 100%) when all four pixels in the 2×2 cell are valid. Transition zones between snow-covered and snow-free areas are particularly problematic. In the future, the aggregation approach to estimating snow fraction may be replaced by a spectral-mixing algorithm [e.g., *Romanov et al*., 2003; *Painter et al*., 2009] or NDSI-based approach [e.g., *Salomonson and Appel*, 2004]. Such a product would be more robust and more attractive to the users.

7. Summary

[59] The VIIRS snow and ice products include the Ice Surface Temperature (IST) EDR, the Sea Ice Characterization EDR, the Sea Ice Concentration IP, and the Snow Cover EDR. The Snow Cover EDR is comprised of two products: a binary snow map and fractional snow cover. Primary operational users of the products in the U.S. are the National Ice Center, the National Operational Hydrologic Remote Sensing Center, the National Centers for Environmental Prediction (NCEP), and the National Weather Service, including the Alaska Ice Desk.

[60] Early validation results are generally positive. The Ice Surface Temperature product is meeting the accuracy requirements, with a root-mean-square (RMS) error of 0.6–1.0 K when compared to aircraft data and a similar MODIS product. The measurement accuracy and precision of VIIRS sea ice concentration retrievals are approximately 5% and 15% when compared to passive microwave retrievals. There is no

accuracy requirement for intermediate products. Sea ice characterization, which consists of two age categories, meets the accuracy requirement for daytime retrievals and some nighttime retrievals but with substantial misclassification during many nighttime scenes.

[61] The accuracy of the binary snow cover maps as compared to the station data is generally above 90% and therefore meets the requirement. The estimated accuracy of VIIRS snow maps is similar to, and may even exceed, the accuracy of snow cover maps derived from MODIS. However, this higher accuracy is partially explained by a more conservative cloud mask provided with the VIIRS snow cover product. The second VIIRS snow EDR, fractional snow cover, is a direct derivative of the binary snow cover map and therefore is of limited utility.

[62] The products are currently at the "provisional" maturity level. Provisional maturity means that product quality may not be optimal; incremental product improvements are still occurring; version control is in affect; the research community is encouraged to participate in the quality assurance (QA) and validation of the product but need to be aware that product validation and QA are ongoing; users are urged to consult the EDR product status document prior to use of the data in publications; and the product is ready for operational evaluation. Further modifications and improvements should be expected as the issues discussed throughout this paper are addressed.

[63] **Acknowledgments.** This work was supported by the JPSS Program Office. The views, opinions, and findings contained in this report are those of the authors and should not be construed as an official National Oceanic and Atmospheric Administration or U.S. Government position, policy, or decision.

References

Baker, N. (2011a), *Joint Polar Satellite System (JPSS) VIIRS Ice Surface Temperature Algorithm Theoretical Basis Document (ATBD), 474–00052*, 40 pp., NASA Goddard Space Flight Center, Greenbelt, Md.

Baker, N. (2011b), *Joint Polar Satellite System (JPSS) VIIRS Snow Cover Algorithm Theoretical Basis Document (ATBD), 474–00038*, 52 pp., NASA Goddard Space Flight Center, Greenbelt, Md.

Baker, N. (2012a), *Joint Polar Satellite System (JPSS) VIIRS Radiometric Calibration Algorithm Theoretical Basis Document (ATBD) Rev. B, 474–00027*, 154 pp., NASA Goddard Space Flight Center, Greenbelt, Md.

Baker, N. (2012b), *Joint Polar Satellite System (JPSS) NPP Operational Algorithm Proxy and Synthetic Test Data Description, 474–0096*, 137 pp., NASA Goddard Space Flight Center, Greenbelt, Md.

Baker, N. (2012c), *Joint Polar Satellite System (JPSS) Operational Algorithm Description Document (OAD) for VIIRS Sea Ice Age (SIA) Environmental Data Records (EDR) Software Rev. A, 474–00087*, 36 pp., NASA Goddard Space Flight Center, Greenbelt, Md.

Baker, N. (2013a), *JPSS VIIRS Cloud Mask Algorithm Theoretical Basis Document (ATBD), Rev B, 474–00033*, 91 pp., NASA Goddard Space Flight Center, Greenbelt, Md.

Baker, N. (2013b), *Joint Polar Satellite System (JPSS) Operational Algorithm Description Document (OAD) for VIIRS Ice Surface Temperature (IST) Environmental Data Records (EDR) Software Rev. B, 474–00072*, 23 pp., NASA Goddard Space Flight Center, Greenbelt, Md.

Bitz, C. M., and W. H. Lipscomb (1999), An energy-conserving thermodynamic model of sea ice, *J. Geophys. Res.*, *104*(C7), 15,669–15,677, doi:10.1029/1999JC900100.

Comiso, J. C. (2002), A rapidly declining perennial sea ice cover in the Arctic, *Geophys. Res. Lett.*, *29*(20), 1956, doi:10.1029/2002GL015650.

Comiso, J. C., D. J. Cavalieri, C. L. Parkinson, and P. Gloersen (1997), Passive microwave algorithms for sea ice concentration: A comparison of two techniques, *Remote Sens. Environ.*, *60*(3), 357–384, doi:10.1016/S0034-4257(96)00220-9.

Drobot, S., J. Stroeve, J. Maslanik, W. Emery, C. Fowler, and J. Kay (2008), Evolution of the 2007–2008 Arctic sea ice cover and prospects for a new record in 2008, *Geophys. Res. Lett.*, *35*, L19501, doi:10.1029/2008GL035316.

Hall, D. K., and G. A. Riggs (2007), Accuracy assessment of the MODIS snow products, *Hydrol. Processes*, *21*, 1534–1547.

Hall, D. K., G. A. Riggs, and V. V. Salomonson (2001), Algorithm Theoretical Basis Document (ATBD) for the MODIS Snow and Sea Ice-Mapping Algorithms. [Available at http://modis-snow-ice.gsfc.nasa.gov/atbd.html.]

Hall, D. K., J. Key, K. A. Casey, G. A. Riggs, and D. J. Cavalieri (2004), Sea ice surface temperature product from the Moderate Resolution Imaging Spectroradiometer (MODIS), *IEEE Trans. Geosci. Remote Sens.*, *42*(5), 1076–1087.

Helfrich, S. R., D. McNamara, B. H. Ramsay, T. Baldwin, and T. Kasheta (2007), Enhancements to, and forthcoming developments in the Interactive Multisensor Snow and Ice Mapping System (IMS), *Hydrol. Processes*, *21*, 1576–1586.

Hutchison, K., and A. P. Cracknell (2006), *Visible Infrared Imager Radiometer Suite—A New Operational Cloud Imager*, 230 pp., CRC Press, Boca Raton, Fla.

Ip, J., and B. Hauss (2009), Pre-launch performance assessment of the VIIRS ice surface temperature algorithm, Fifth Annual Symposium on Future Operational Environmental Satellite Systems NPOESS-GOES-R, 16th Conference on Satellite Meteorology and Oceanography, 89th Annual American Meteorological Society Annual Meeting, Phoenix, Ariz., January.

Johannessen, O. M., et al. (2004), Arctic climate change: Observed and modeled temperature and sea-ice variability, *Tellus, Ser. A*, *56*, 328–341.

Key, J., and M. Haefliger (1992), Arctic ice surface temperature retrieval from AVHRR thermal channels, *J. Geophys. Res.*, *97*(D5), 5885–5893.

Key, J., J. Collins, C. Fowler, and R. Stone (1997), High-latitude surface temperature estimates from thermal satellite data, *Remote Sens. Environ.*, *61*, 302–309.

Klein, A. G., D. K. Hall, and G. A. Riggs (1998), Improving snow cover mapping in forests through the use of a canopy reflectance model, *Hydrol. Processes*, *12*, 1723–1744.

Kurtz, N., J. Richter-Menge, S. Farrell, M. Studinger, J. Paden, J. Sonntag, and J. Yungel (2013), IceBridge airborne survey data support arctic sea ice predictions, *Eos Trans. AGU*, *94*(4), 41, doi:10.1002/2013eo040001.

Kwok, R., and G. F. Cunningham (2008), ICESat over Arctic sea ice: Estimation of snow depth and ice thickness, *J. Geophys. Res.*, *113*, C08010, doi:10.1029/2008JC004753.

Kwok, R., G. F. Cunningham, M. Wensnahan, I. Rigor, H. J. Zwally, and D. Yi (2009), Thinning and volume loss of the Arctic Ocean sea ice cover: 2003–2008, *J. Geophys. Res.*, *114*, C07005, doi:10.1029/2009JC005312.

Maslanik, J. A., C. Fowler, J. Stroeve, S. Drobot, J. Zwally, D. Yi, and W. Emery (2007), A younger, thinner Arctic ice cover: Increased potential for rapid extensive sea-ice loss, *Geophys. Res. Lett.*, *34*, L24501, doi:10.1029/2007GL032043.

Massom, R., and J. C. Comiso (1994), The classification of Arctic sea ice types and the determination of surface temperature using advanced very high resolution radiometer data, *J. Geophys. Res.*, *99*(C3), 5201–5218.

National Ice Center (2008), *IMS Daily Northern Hemisphere Snow and Ice Analysis at 4 km and 24 km Resolution*, National snow and ice data center, Boulder, Colo., doi:10.7265/N52R3PMC.

Painter, T. H., K. Rittger, C. McKenzie, P. Slaughter, R. E. Davis, and J. Dozier (2009), Retrieval of subpixel snow covered area, grain size, and albedo from MODIS, *Remote Sens. Environ.*, *113*, 868–879.

Romanov, P., D. Tarpley, G. Gutman, and T. R. Carroll (2003), Mapping and monitoring of the snow cover fraction over North America, *J. Geophys. Res.*, *108*(D16), 8619, doi:10.1029/2002JD003142.

Salomonson, V. V., and I. Appel (2004), Estimating fractional snow cover from MODIS using the normalized difference snow index, *Remote Sens. Environ.*, *89*, 351–360.

Vermote, E., D. Tanré, J. L. Deuzé, M. Herman, and J. J. Morcrette (1997), Second simulation of the satellite signal in the solar spectrum, 6S: An overview, *IEEE Trans. Geosci. Remote Sens.*, *35*(3), 675–686.

Wang, X., H. Xie, T. Liang, and X. Huang (2008), Comparison and validation of MODIS standard and new combination of Terra and Aqua snow cover products in northern Xinjiang, China, *Hydrol. Processes*, *23*, 419–429.

Wang, X., J. R. Key, and Y. Liu (2010), A thermodynamic model for estimating sea and lake ice thickness with optical satellite data, *J. Geophys. Res.*, *115*, C12035, doi:10.1029/2009JC005857.

Yu, Y., and D. A. Rothrock (1996), Thin ice thickness from satellite thermal imagery, *J. Geophys. Res.*, *101*(C10), 25,753–25,766.

Yu, Y., D. A. Rothrock, and R. W. Lindsay (1995), Accuracy of sea ice temperature derived from the advanced very high resolution radiometer, *J. Geophys. Res.*, *100*, 4525–4532.

Zhang, J., and D. A. Rothrock (2003), Modeling global sea ice with a thickness and enthalpy distribution model in generalized curvilinear coordinates, *Mon. Weather Rev.*, *131*(5), 681–697.

Zwally, H. J., D. Yi, R. Kwok, and Y. Zhao (2008), ICESat measurements of sea ice freeboard and estimates of sea ice thickness in the Weddell Sea, *J. Geophys. Res.*, *113*, C02S15, doi:10.1029/2007JC004284.